# Sensitivity of LES predictions of wind loading on a high-rise building to the inflow boundary condition

Giacomo Lamberti[a,*], Catherine Gorlé[a]

[a] *Stanford University, Y2E2 Building, 473 Via Ortega, Stanford, CA, 94305*

---

## Abstract

Large eddy simulations (LES) can provide a powerful tool for cladding design, but their accuracy strongly depends on the correct representation of the incoming atmospheric boundary layer (ABL). The objective of this work is to validate LES of a wind tunnel experiment of wind loading on a high-rise building, focusing on accounting for sensitivity to the incoming ABL. We define three uncertain parameters, i.e. the roughness length of the terrain, the turbulence kinetic energy, and the integral time-scale, using the available experimental data. Subsequently we perform 27 LES using different combinations of these parameters. The results indicate that (1) accurately quantifying the turbulence statistics at the building location, rather than at the inflow, is essential when analyzing LES of wind loading, and (2) correctly accounting for inflow uncertainty when performing validation against experiments could drastically improve confidence in the predictions. By accounting for this uncertainty, we predict intervals that encompass the experimental data for the rms pressure coefficients. The magnitude of the local peak pressure coefficients is generally under-predicted by 12%; however, the predicted intervals for design pressure coefficients on cladding panels of different sizes located at the upper-windward corner of the building fully encompass the experimental result.

*Keywords:* Large-eddy simulations (LES), wind loading, uncertainty quantification (UQ)

---

[*] Corresponding author

*Email addresses:* `giacomol@stanford.edu` (Giacomo Lamberti), `gorle@stanford.edu` (Catherine Gorlé)

*Preprint submitted to Elsevier* *January 4, 2021*

## 1. Introduction

Cladding design requires accurate estimations of wind loads to guarantee the structural integrity of cladding panels without resorting to overly conservative designs. This is especially important near the corners and edges of high-rise buildings' side walls, where the wind-induced pressure is characterized by a strong non-Gaussian behavior [1–6] that can result in extreme suction loads. The most common approach to estimate wind loads for cladding design relies on wind tunnel experiments. During cladding experiments, a synchronous multi-pressure sensing system (SMPSS) records pressure time series in several locations on the building's surface [7–14]. The main limitation of this type of tests lies in the spatial resolution of the measurements. The number of pressure taps that is used in routine wind tunnel tests is insufficient to accurately estimate the area-averaged pressure on each cladding panel from integration of the local pressure distribution. Therefore, alternative methods have been developed to estimate the area-averaged pressure from limited measurement locations. A common approach is to assume a linear relationship between the duration and spatial extension of the pressure peak phenomena. Under this assumption, the pressure time-series can be filtered to remove extremely localized peak events that are not relevant for cladding design [15–17]. However, the assumption of a linear relationship between the duration and the size of peak events can introduce inaccuracies in the calculated design loads [18].

Computational fluid dynamics (CFD) represents an attractive alternative in this respect: the required resolution for the simulations generally results in a sufficient number of grid cells within the area of a typical cladding panel to directly calculate the total load from integration. Large-eddy simulations (LES), which apply a low-pass filter to the Navier-Stokes equations to resolve the larger energy-containing scales of turbulence, such that only the smaller, more universal scales need to be modeled [19], are of particular interest: the simulations allow for a direct estimate of the design pressure coefficients based on the time-series of the resolved pressure coefficients. However, LES results can depend on specific model choices, such as the numerical schemes, the turbulence model, or the inflow boundary conditions. The importance of the inflow conditions has been clearly demonstrated on two benchmark test cases. In [20], 70 simulations and experiments of pressure coefficients on a rectangular cylinder were compared, while [21] reviewed LES and experiments on the high-rise CAARC building. In both cases significant discrepancies were observed between the different experimental and numerical results on the lateral faces (or façades), and it was suggested that differences in the inflow conditions could be responsible for these discrepancies. Several other studies also concluded that good agreement between LES and experimental results is strongly dependent on the accuracy of the specified inflow conditions [22–26].

The definition of a turbulent inflow condition that accurately represents the surface layer in terms of the mean velocity, turbulence intensities, and turbulence length-scales, can be particularly challenging in LES. Synthetic turbulence generators are a popular choice because of their computational efficiency, but results depend both on the specific turbulence generator used and on the required input parameters. [23] performed LES on the CAARC building using three different inflow methods and demonstrated significant scatter in the predicted mean and root-mean-square (rms) pressure coefficients in the separation region. [27] performed LES simulations of a high-rise building, using a synthetic turbulence generator. They considered 2 different velocity and turbulence intensity profiles, and showed that the specified mean velocity profile mainly influences the mean pressure on the building, while the prescribed turbulence intensity has a stronger effect on the pressure fluctuations. [28] used a different synthetic turbulence generator to perform several LES simulations, considering baseline and halved values for the turbulence intensity and integral length-scales. The authors concluded that the specified integral length-scales have a smaller effect on the mean and rms pressure coefficients on the building's surface compared to the turbulence intensity.

The analysis of the dependence of LES results on the specific formulation of the turbulence generator and the selected input parameters is further complicated by the fact that the specified inflow statistics will develop towards an equilibrium solution downstream of the inlet. The generated turbulent velocity field is not a solution of the system of equations being solved, and the final result at the location of the building will depend on the subgrid model, the wall model, and the discretization used. It is not uncommon to observe a strong decrease in the turbulence intensity between the inlet and the downstream location of interest [29, 30]. As a result, it is difficult to generalize the conclusions of previous studies, since the precise turbulent velocity statistics at the location of the building are unknown. In [31] we proposed to address this problem by optimizing the input parameters of a divergence-free digital filter turbulent inlet generator [32], such that the desired velocity statistics are obtained at the location of the building.

The goal of the present work is to leverage this method to investigate the effect of uncertainty in the inflow conditions on LES predictions of the mean, rms and peak pressure coefficients on a high-rise building in a systematic way. We model a wind tunnel experiment that provides high-resolution pressure measurements on the building's lateral façades[18, 33], since previous studies indicated high sensitivity of the results to the inflow conditions in these locations. We focus on the effect of three uncertain parameters that define the incoming surface layer: the roughness length of the terrain, the turbulence kinetic energy and the integral time-scale of the streamwise velocity component. These parameters are characterized using the available wind tunnel measurements, and the inflow optimization is performed to identify 27 realizations of digital filter input parameters that represent the variability in the wind tunnel flow conditions. The ensemble of the 27 LES results is then analyzed to assess uncertainty in the predicted mean, rms and peak pressure coefficients. We consider both local peak pressure coefficients and design pressure coefficients averaged over different panel sizes, which are the quantities of interest for cladding design. The results are compared to the wind tunnel data for validation, and additional analysis is performed to provide insight on the relative importance of the different uncertain inflow parameters.

The remainder of this paper is organized as follows: Section 2 summarizes the wind tunnel experiment, while Section 3 presents the LES setup and the details of the inflow sensitivity analysis. In Section 4, we present the results, and Section 5 summarizes the conclusions and identifies possible areas of future research.

## 2. Wind tunnel measurements

The simulations model a wind tunnel experiment on a high-rise building, carried out in the closed-section wind tunnel of Politecnico di Milano (PoliMi) [18]. The facility has a test section that is 35m long, 14m wide and 4m high. In this section, we briefly summarize the velocity measurements, performed to characterize the atmospheric boundary layer (ABL) in the wind tunnel, and the pressure measurements on the building. For additional details regarding the experiments the reader is referred to [18, 33].

### *2.1. ABL characterization*

A detailed characterization of the ABL was performed using 3D hot-wires with a sampling frequency of 2000Hz. The velocity components were recorded on a plane perpendicular to the flow direction at the center of the turntable, i.e. at the future location of the building model. The outcome of the experiments consists of 20s time-series of the three components of velocity at 5 spanwise locations and 56 vertical locations. The 5 spanwise locations are 0.6m apart, while the resolution in the vertical direction is 43.7mm below 0.75m and 87.5mm above, as indicated in Figure 1.

### *2.2. Pressure measurements*

The model of the high-rise building, shown in Figure 2, is a 1m long, 0.3m wide and 2m high rectangular box. The experiment was designed to enable a detailed study of the pressure distribution in the regions of the building where the highest pressure peaks are expected, i.e. near the corners and edges of the building. Therefore, the model was equipped with 2 aluminum tiles containing 224 pressure taps each, with a minimum spacing of 3.4mm. Tile A is located on

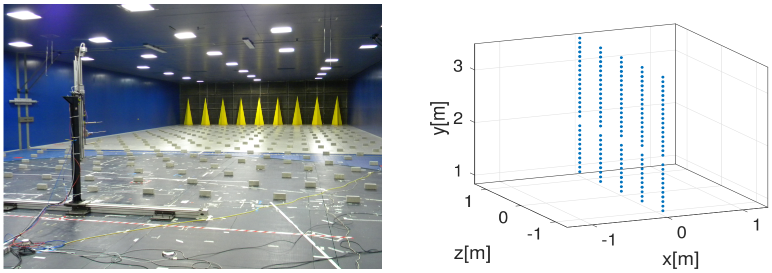

(a) Setup of the experiment to characterize the ABL at PoliMi

(b) Coordinates of the hot-wire measurements

Figure 1: PoliMi experimental setup of velocity measurements.

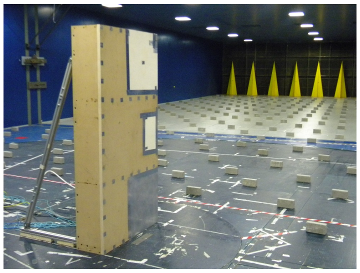

Figure 2: Test on the high-rise building

the top-corner of the model while tile B is centered at 1m height and adjacent to the building edge (Figure 3b). The outcome of the experiment consists of 300s long time-series of pressure, sampled at a rate of 500Hz.

The high-rise building model was placed at the center of a turntable with a radius of 6.5m, to allow testing at different inflow directions. In the present work we focus on the standard 0° exposure, following the convention defined in Figure 3a. Using the symmetry of the model, the wind tunnel data obtained for the 180° exposure will be used for a more complete validation of the predicted lateral façade pressure coefficients for 0° exposure.

## 3. Methods

### *3.1. CFD model set-up*

All LES simulations are performed with the OpenFOAM v4.0 pisoFOAM solver, using the standard Smagorinsky subgrid-scale turbulence model [34]. The Reynolds number of the flow, based on the building height and the reference

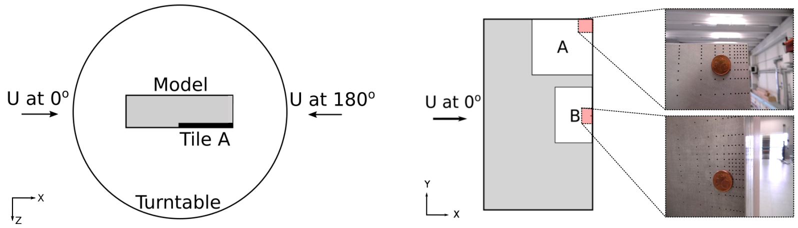

(a) Top view of the turntable, indicating the convention used for the wind direction (b) Side view of the building model and the pressure tap distribution

Figure 3: High-rise building pressure measurements setup.

velocity at the building height, is ∼ 1.1 million. The computational domain is 20 × 5m in the streamwise and spanwise directions; the height of the domain is equal to the wind tunnel height, i.e. 4m. The high-rise building is located at a distance of 5m from the inlet boundary and 14m from the outlet [23]. The blockage ratio, i.e. the ratio between the area of the windward face of the building and the domain cross section, is 2.8% [35].

The mesh includes refinement regions close to the ground and to the building model, resulting in a total number of 7.5 million hexahedral cells. The highest spatial resolution is achieved next to the corners of the building, similar to the pressure tap distribution in the wind tunnel experiment. In these regions, the resolution is 3.2mm, 1.6mm and 0.8mm in the streamwise, spanwise, and vertical directions, respectively, which result in $y^+ \sim 100$ on average. Since the wall-adjacent cells extend into the logarithmic region, a log law wall function is used to fit the instantaneous horizontal velocity and predict the wall shear stress on the building surface [36]. To investigate the effect of the chosen grid resolution, a simulation was performed with a coarser mesh, which had a 4 times lower spatial resolution next to the corners and edges of the building. The predictions for the mean pressure coefficient had a coefficient of agreement $R^2 = 0.97$, while for the rms pressure coefficients $R^2 = 0.83$. Power spectral densities of the pressure signals presented in Section 4 further indicate that the finer grid resolves the scales that contribute most to the pressure fluctuations.

To generate a turbulent flow field at the inflow, we employ the divergence-free version of the digital filter method developed in [32, 37]. The method introduces a turbulent velocity field in a plane next to the inlet boundary, as follows:

$$u_i = U_i + a_{ij} u_{*,j}, \tag{1}$$

where $U_i$ is the mean velocity, $a_{ij}$ the Cholesky decomposition of the Reynolds stress tensor and $u_{*,j}$ a random fluctuation with zero mean and exponential spatial and temporal correlation. As proposed in [31], the inflow generation method is coupled with an optimization algorithm to ensure that the desired turbulence statistics are obtained at the location of the building; this is discussed in more detail in section 3.2. At the lower wall, a rough-wall logarithmic wall function, designed to guarantee horizontal homogeneity of the mean velocity profile, is applied. The formulation is similar to the wall function commonly used in RANS simulations of the ABL [38, 39], but it is applied to the instantaneous flow field [36].

On the side boundaries we impose periodic boundary conditions, while on the top boundary we impose a slip boundary condition. The outlet is treated as a pressure-outlet with constant relative pressure equal to zero and a zero-gradient boundary condition for the other flow variables. The momentum and turbulence model equations are discretized using second order numerical schemes and iteratively solved using a linear solver with a symmetric Gauss-Seidel smoother. The Poisson equation is approximated with second order schemes and solved using the generalised geometric-algebraic multi-grid (GAMG) solver with Gauss-Seidel smoother. To monitor convergence of the time-statistics, we select 1 pressure tap per pressure tile and run the simulations until the corresponding mean and rms pressure coefficients stopped varying. After this burn-in period, we further run the simulations for $50 - 60$s to obtain the pressure time-series, with a 0.0001s time-step.

### *3.2. Characterization of the inflow uncertainty*

The objective is to quantify the effect of inflow uncertainty in the experiment by performing an ensemble of LES simulations. We characterize the inflow uncertainty by considering the spanwise variation in the measured profiles for the mean velocity, the turbulence kinetic energy, and the streamwise integral time scales, as shown by the grey shaded area in Figure 4. Subsequently, three different profiles are defined for each of these quantities, covering the range of the measured values.

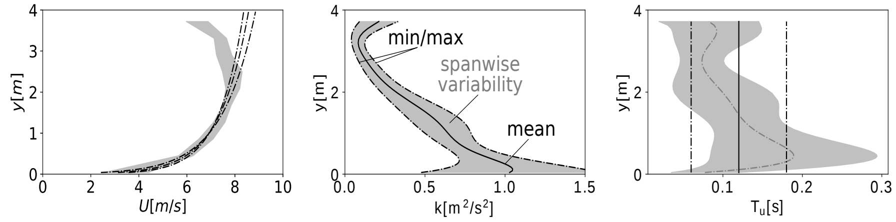

(a) Mean streamwise velocity (b) Turbulence kinetic energy (c) Streamwise integral time scale

Figure 4: ABL profiles for the inflow sensitivity analysis.

The mean velocity profile is prescribed using the log-law, which is determined by two independent parameters: a reference velocity and the roughness length of the terrain $y_0$. Since we can expect the pressure coefficients to be Reynolds number independent, we select $y_0$ as the uncertain parameter. By fitting a logarithmic profile to the measurements at each spanwise location, we define an upper and lower limit and a mean value for $y_0$; the resulting mean velocity profiles are shown in Figure 4a. These profiles are used to define $U_i$ in Eq. 1; by using the wall function that represents the effect of the roughness length of the terrain we ensure that the shape of the inlet profile is maintained throughout the domain [31].

The three profiles for the turbulence kinetic energy are defined by considering the minimum, mean and maximum values from the measurements. To compensate for the turbulence decay commonly observed when using digital filter methods, we first perform simulations for an empty domain with the optimization algorithm proposed in [31]. The optimization procedure adjusts the input parameters for the inflow generator until the desired statistics are obtained at the location of interest. In particular, to achieve turbulence intensities at the building location that closely represent the experimental values, the algorithm modifies the spanwise ($\overline{w'^2}$) and vertical ($\overline{v'^2}$) components of the Reynolds stress tensor imposed at the inflow. The optimization was performed for the mean values of $y_0$ and the integral time scale (discussed next), providing three sets of inputs for $a_{ij}$ in Eq. 1 that can represent the three profiles plotted in 4b.

The last term in Eq. 1 is the fluctuation term $u_{*,j}$, which is a function of the turbulence integral length- and time-scales. Since the spatial resolution of the hot-wire measurements is insufficient to compute 2-point correlations, we used Taylor's hypothesis [40] to compute the integral length-scales [31]. The streamwise integral time-scale $T_u$ was then selected as the third uncertain parameter. Upper and lower bounds, and the mean value for the parameter are shown in Figure 4c; in this case the inflow algorithm requires a constant value over height [31]. The resulting values for $T_u$ are directly used to specify the temporal correlation of $u_{*,j}$ at the inlet. It is noted that some streamwise inhomogeneity in the time scales has been observed. This variation is more challenging to control using the optimization, in part because the value specified at the input can also affect the downstream level of turbulence kinetic energy. This interaction will be quantified in section 4.2, and it will be taken into account when interpreting the results for the pressure coefficients.

In summary, we represent the uncertainty in the inflow conditions using three parameters: the roughness length of the terrain $y_0$, the turbulence kinetic energy $k$ and streamwise integral time-scale $T_u$. The spanwise variation of the experiment was used to characterize these uncertain parameters, defining upper and lower bounds and mean values. All possible combinations of the selected parameter values define 27 inflow conditions; therefore, we perform the corresponding 27 LES simulations to study the effect of the inflow uncertainty on the results.

### 3.3. *Quantities of interest*

#### 3.3.1. *Pressure coefficient time statistics*

We will consider the effect of the different inflow conditions on the statistics of the non-dimensional pressure coefficient, defined as follows:

$$C_p(t) = \frac{p(t) - p_{ref}}{\frac{1}{2}\rho U^2} \tag{2}$$

where $p$ is the instantaneous pressure, $p_{ref}$ the reference pressure, $\rho$ the density of the air and $U$ the reference velocity at roof height. The mean, rms and peak pressure coefficients are given by:

$$C_P = \frac{P}{\frac{1}{2}\rho U^2}, \qquad C'_p = \frac{\sqrt{\overline{p'^2}}}{\frac{1}{2}\rho U^2}, \qquad \check{C}_p = \frac{\check{p}}{\frac{1}{2}\rho U^2} \tag{3}$$

where $P$ and $p'$ represent the mean and fluctuating pressures, respectively, and $\check{p}$ is the peak pressure calculated using the Cook and Mayne method [16]. The peak values relative to a 22% probability of exceedance will be reported; they are calculated by dividing the time-series of $C_p$ in 6s windows, extracting the most negative peak from each window, and fitting a Gumbel distribution to the extreme values.

The quantity that ultimately determines the dimensioning of the panels in cladding design, is the area-averaged pressure coefficient:

$$C_{p,AA}(t) = \frac{\sum_i C_{p,i}(t) A_i}{\sum_i A_i} \tag{4}$$

where $C_{p,i}$ is the pressure coefficient measured by tap $i$ and $A_i$ is the area of influence of tap $i$. From both experimental and LES data, we compute $C_{p,AA}$ for panels of different size and apply the Cook and Mayne method as described above, to calculate the design pressure coefficient of the panels $\check{C}_{p,d}$, relative to a 22% probability of exceedance.

## 4. Results

In this section, we first present an initial analysis of the LES simulation with the mean inflow parameters. This analysis focuses on comparing the spectra and characteristics of the time series and peak events of the pressure coefficients to the wind tunnel data to confirm that the energy-containing turbulence scales are sufficiently resolved by the LES. Subsequently, we analyze the ABL velocity statistics at the building location in all 27 LES, to confirm that the ensemble of simulations can represent the uncertainty in the inflow conditions of the wind tunnel experiment. Finally, we present the results for the pressure coefficients obtained from the ensemble of LES. Predictions for the mean, rms, peak and design pressure coefficients are compared to the wind tunnel data for validation, and analyzed to identify the relative importance of the uncertain inflow parameters.

### *4.1. Analysis of baseline LES pressure coefficient spectra, time-series, and peak events*

Figure 5 shows an instantaneous snapshot of the velocity magnitude field obtained from the baseline LES simulation with the mean inflow parameters. Turbulent structures are produced at the inflow generation plane and advected downstream to the building model. A stagnation region is formed just upstream of the windward façade; there is separation on the lateral façades and a wake forms behind the building. The top view of Figure 5 indicates the presence of vortex shedding, but the high turbulence intensity of the inflow prevents pronounced periodic behavior. The remainder of this section analyzes the predictions for the pressure coefficients on the building lateral façade, to verify that the LES can adequately resolve the turbulent wind pressure field. First, we present pressure spectra and time-series of pressure coefficients, measured at pressure taps in locations where strong negative pressure peaks occur. Subsequently, contours of instantaneous $C_p$ over a panel next to the top corner of the building during a pressure peak event are plotted, and related to the presence of coherent turbulence structures in the flow.

Figure 6 shows the non-dimensional power spectra of the pressure coefficient measured at four pressure taps near the corners of the building, computed using Welch method [41]. The result of the baseline LES is compared to the wind tunnel measurements. The spectra compare well in the energy-containing range

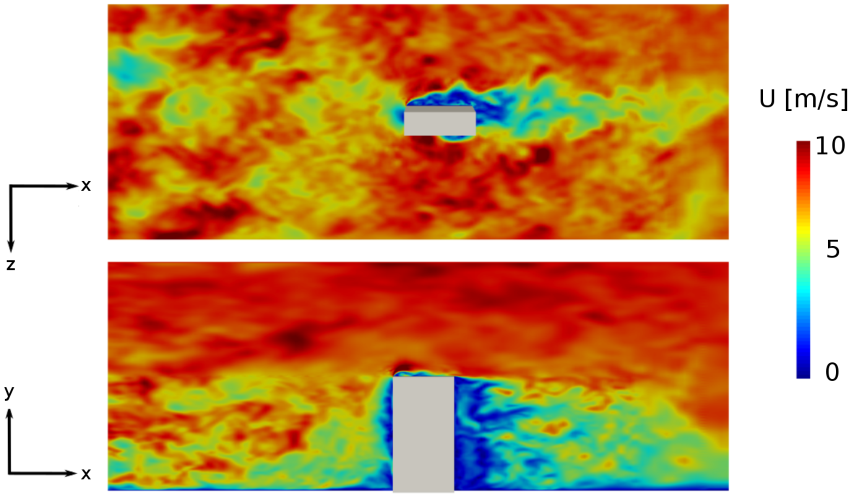

Figure 5: Contour plot of instantaneous velocity magnitude from the baseline LES simulation.

and in the first part of the inertial subrange. At non-dimensional frequencies $\frac{fB}{U} > 1$ (where $f$ is the dimensional frequency, $B$ the width of the building and $U$ the reference velocity at roof height), the energy in the LES simulation drops, indicating that these higher frequencies can not be resolved. The pressure tap at mid-height near the downwind corner of the model (Figure 6f), exhibits a peak in the power spectrum of both the experiment and the LES, at $\frac{fB}{U} \sim 0.15$; this is likely related to vortex shedding.

Figure 7 plots a 50s time-series of the pressure coefficient recorded at a pressure tap next to the windward top corner of the building; this is where the strongest suction peaks occur for the wind direction under consideration. The two time-series exhibit very similar behavior, characterized by the occurrence of several negative pressure coefficient peaks. Specifically, 6 and 3 peaks lower than $C_p = -2$ are experienced in the LES and the experiment respectively. The strongest negative peak recorded by the selected pressure tap is $\sim -2.8$ in the LES and $\sim -2.7$ in the experiment. When considering the full 300s duration of the experiment, the largest negative peak measured at the same pressure tap is $\sim -3.5$. In section 4.3, the peak values for a 22% probability of exceedance will be calculated using the Cook and Maine method to enable a statistically

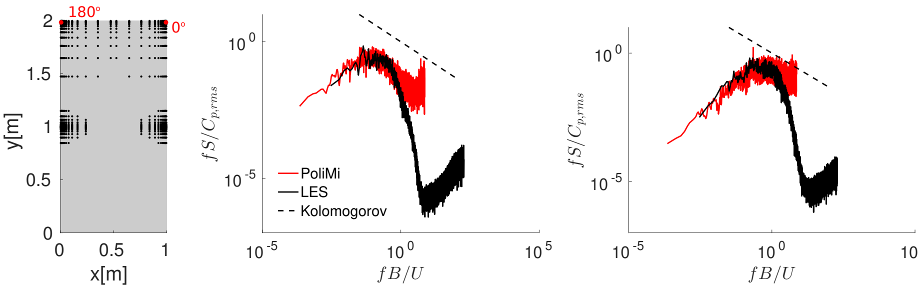

(a) Top-corner tap (b) power spectral density at 180° (c) power spectral density at 0°

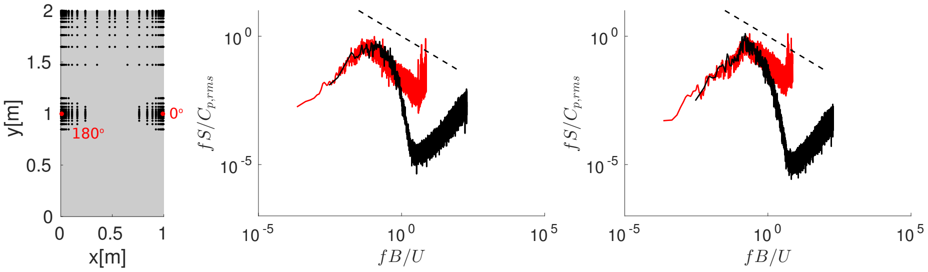

(d) Mid-edge tap (e) power spectral density at 180° (f) power spectral density at 0°

Figure 6: Power spectral density on top-corner and mid-edge taps.

meaningful comparison of the peak values.

To visualize the nature of the pressure peak events, Figure 8 shows the distribution of the instantaneous $C_p$ near the windward upper corner of the building during a peak event. The time-series of $C_p$ measured by two taps near the location of the peak event are also plotted and compared to the area-averaged $C_p$ of a $2 \times 3\text{m}^2$ panel. The plots demonstrate the similar nature of the pressure peak events in the wind tunnel experiment and the LES simulation. A region of pressure coefficients lower than $-2.5$ appears next to upper corner of the windward edge of the building, around the same pressure tap (*tap1*). The time-series of $C_p$ measured by *tap1* reaches a negative value of $\sim -2.8$, in both the LES and the experiment (Figures 8b and 8e). The duration of the peak event is $\sim$ 395ms in the LES simulation, while it is $\sim$ $188ms$ in the experiment. The LES signal is smoother than the experimental one, which confirms the observation from the spectra (Figure 6) that the LES cannot resolve the smallest turbulent scales observed in the experiment. When calculating the

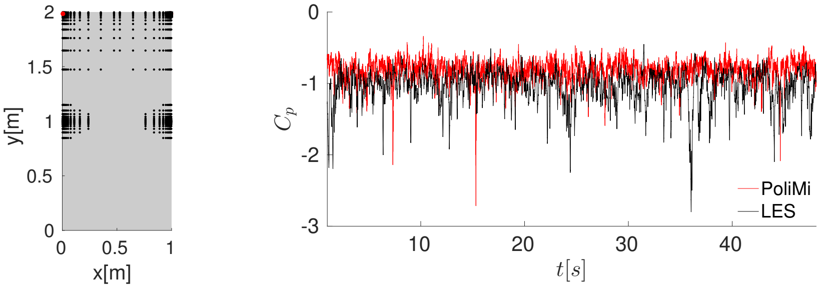

(a) Top-corner tap

(b) Time-series of $C_p$

Figure 7: Time-series of pressure coefficient on top-corner tap.

area-averaged values of $C_p$, the peak values drop from $\sim -1$ to $\sim -1.6$ in both the LES and the experiment; this indicates the importance of considering the pressure loads averaged over an area of interest in addition to the local peak values.

Lastly, Figure 9 relates the peak pressure events to the flow features by plotting the instantaneous $C_p$ distribution on the entire side wall together with the simultaneous contour of the second invariant of the velocity gradient tensor $Q$ [42]. Coherent structures corresponding to $Q = 2,000\text{s}^{-2}$ are presented and colored by the instantaneous $C_p$. They visualize how the shear layer formed near the upwind corner of the model separates and rolls up into large vortices, which cause regions of relatively strong suction further downstream [43]. This effect is strongest near the top of the building, where the interaction between shear layers originating from the upwind and top corners generates the highest suctions.

### *4.2. ABL velocity statistics*

In Figure 10, we compare the 27 LES results for the turbulent velocity statistics at the building location to the wind tunnel measurements. The spread of the profiles is significant, especially in terms of the turbulence kinetic energy and integral time-scale (Figures 10b and 10c). The ensemble of LES profiles provides a good representation of the spanwise variation in the wind tunnel experiment above 0.25m height. Closer to the ground, the turbulence kinetic

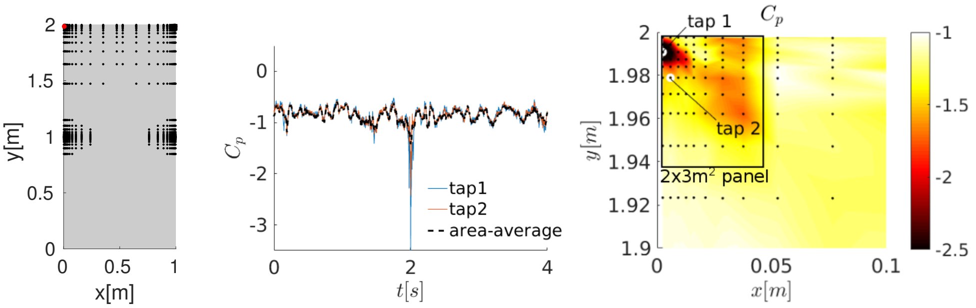

(a) Top-corner taps (b) PoliMi: $C_p$ time-series (c) PoliMi: $C_p$ contour

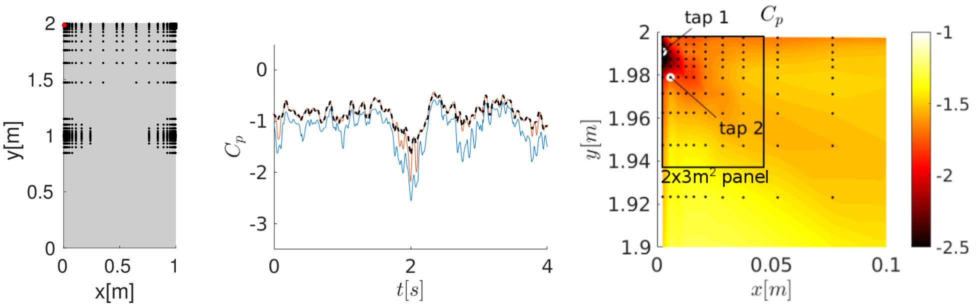

(d) Top-corner taps (e) LES: $C_p$ time-series (f) LES: $C_p$ contour

Figure 8: Time-series of pressure coefficient on top-corner tap and pressure coefficient distribution on the tile at the time instant of the negative peak.

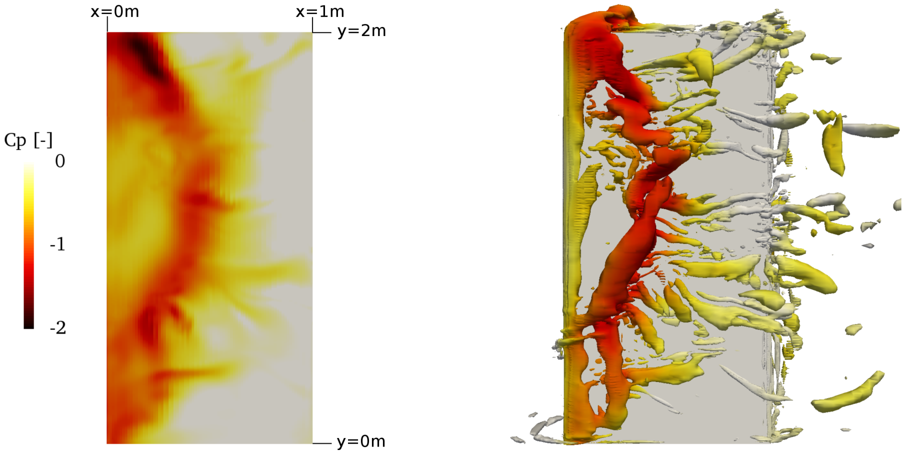

Figure 9: Contours of instantaneous pressure coefficient and iso-surface of the second invariant of the velocity gradient tensor $Q = 2,000\text{s}^{-2}$, colored by the instantaneous pressure coefficient.

energy is underpredicted, while the integral time-scales are overpredicted. The former can be explained by the fact that the experimental uncertainty in the turbulence kinetic energy significantly increases next to the ground, while the latter by the fact that the inflow generation method assumes profiles of integral time-scales that are constant over height. The behavior is similar to the one observed in [31]

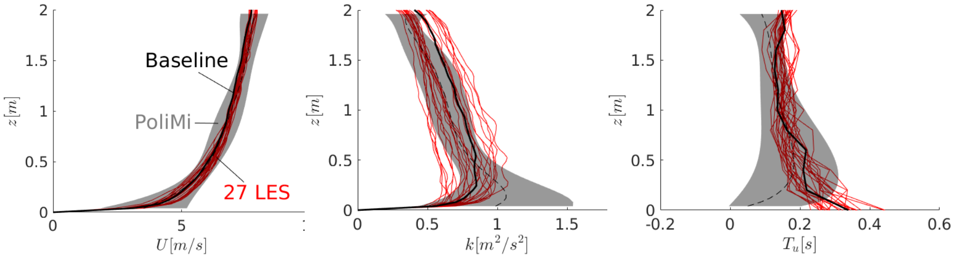

(a) Mean streamwise velocity (b) Turbulence kinetic energy (c) Streamwise integral time scale

Figure 10: Turbulence statistics at the building location from the ensemble of LES.

To identify the main effect associated with each input parameter, Figure 11 shows the profiles obtained by averaging the results of the simulations that have a fixed value for one of the uncertain inflow parameters. For example, in the top row of Figure 11, the blue profiles are obtained by averaging the results of the 9 simulations that use the minimum value for the roughness length; similarly, the black and red profiles represent the average of the velocity statistics across the 9 simulations with the mean and maximum values for $y_0$, respectively. In the mid and bottom rows of Figures 11, analogous plots are obtained for different inflow values of the turbulence kinetic energy and the integral time-scale.

The roughness length of the terrain produces the expected effect on the mean velocity profiles (Figure 11a): lower roughness corresponds to higher velocity next to the ground. The terrain roughness has almost no effect on the velocity fluctuations at the building location, as evident from the almost overlapping profiles of Figures 11b and 11c. In contrast, the turbulence kinetic energy and integral time-scale specified at the inflow have a negligible effect on the mean velocity profiles (Figures 11d and 11g), but they affect the turbulence

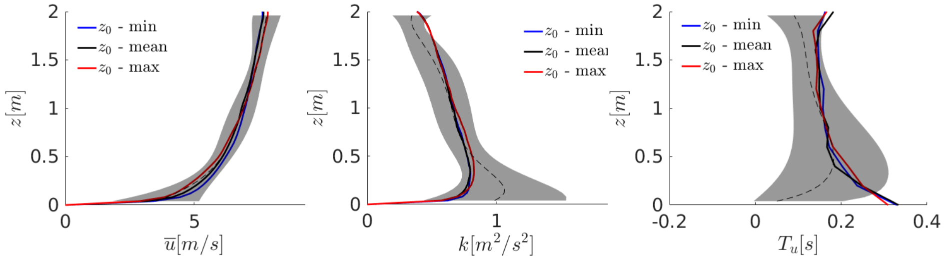

(a) Mean streamwise velocity: effect of $y_0$ (b) Turbulence kinetic energy: effect of $y_0$ (c) Streamwise integral time scale: effect of $y_0$

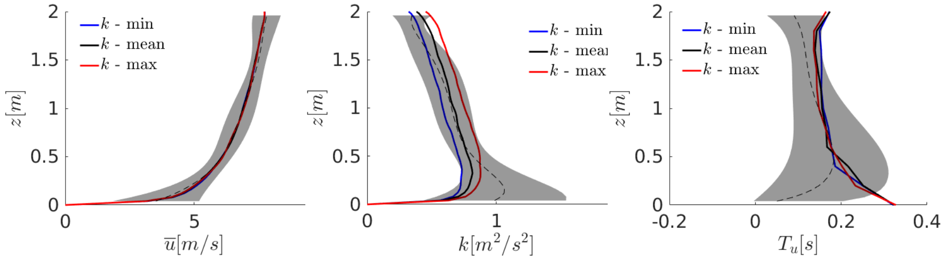

(d) Mean streamwise velocity: effect of $k$ (e) Turbulence kinetic energy: effect of $k$ (f) Streamwise integral time scale: effect of $k$

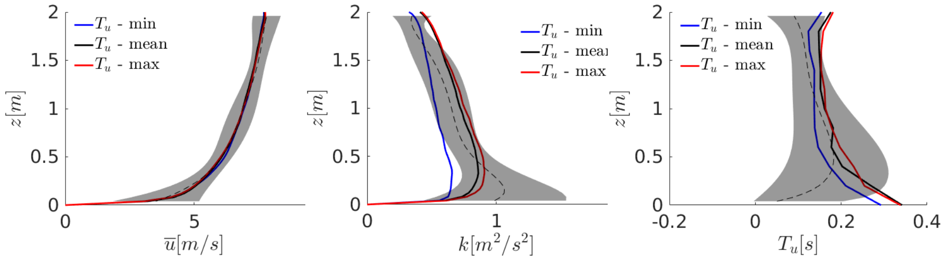

(g) Mean streamwise velocity: effect of $T_u$ (h) Turbulence kinetic energy: effect of $T_u$ (i) Streamwise integral time scale: effect of $T_u$

Figure 11: Effect of the different uncertain inflow parameters on the turbulence statistics at the building location, visualized using profiles averaged over nine simulations with a fixed value for one of the parameters. Comparison to the spanwise-average (dashed line) and the spanwise variation (gray region) of the measurements.

characteristics at the building. Figures 11e and 11f indicate that the level of turbulence kinetic energy can be modified without affecting the integral time scales, while Figures 11f and 11i show that the integral time-scale has a strong interaction effect. This interaction effect should be taken into account when analyzing the results; any variation in the results between the simulations with different time-scales is likely to be strongly affected by the corresponding variation in turbulence kinetic energy at the building location. All observed effects are monotonic: a higher turbulence kinetic energy or time-scale at the inflow results in higher values further downstream. For the integral time-scale there appears to be an upper limit, since an inflow value higher than the experimental mean has little effect on the turbulence statistics further downstream.

### *4.3. Pressure statistics*

#### *4.3.1. Mean pressure coefficient*

Figure 12 shows the mean pressure coefficient distribution on the building's lateral façade from the wind tunnel experiment and the baseline LES. To quantify the sensitivity to the inflow conditions, the discrepancy between the minimum and maximum values recorded across the 27 LES simulations is shown. The wind tunnel and LES data exhibit the same qualitative features: the flow separates at the windward edge of the building, generating a region of relatively strong suction in the separated flow region (red region of Figures 12a and 12b); further downstream, the flow reattaches, reducing the strength of the suction (yellow region of Figures 12a and 12b). The maximum difference in the $C_P$ values predicted from the ensemble of LES simulations occurs in the separation region, next to the top edge, where it reaches $\sim 0.16$ (Figure 12c). This corresponds to a $\sim 20\%$ difference in the predicted mean $C_p$ in this region, indicating that the uncertainty in the inflow conditions has a non-negligible effect on the mean pressure distribution in regions of flow separation

To provide a more quantitative comparison, profiles of the mean pressure coefficient along two rows of taps on the top portion of the model are plotted in Figure 13. The baseline LES result and the sensitivity interval, i.e. the minimum and maximum values across the 27 LES simulations, are compared to the wind

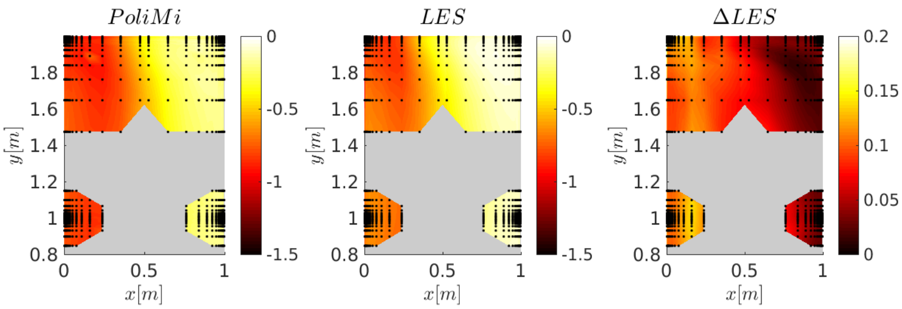

(a) Wind tunnel (b) Baseline LES (c) Maximum discrepancy

Figure 12: Mean pressure coefficient distribution on the building's lateral façade.

tunnel measurements. The ensemble of LES simulations seems to slightly underpredict the magnitude of the mean $C_p$ (Figure 13); the maximum discrepancy between the minimum value of the sensitivity interval and the measurements along the rows of taps considered, is 0.09 on tile A (Figure 13a) and 0.12 on tile B (Figure 13b). The size of the sensitivity intervals confirms that the mean $C_p$ is more sensitive to the inflow uncertainty in the regions of flow separation; in the rear portion of the model, where the flow is attached, the inflow uncertainty has a negligible effect on the quantity of interest.

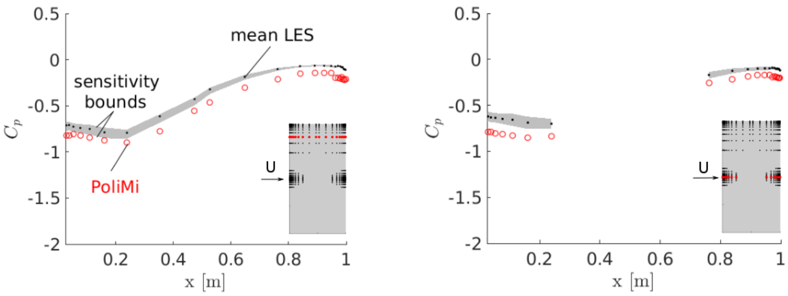

(a) Profiles of $C_P$ (b) Profiles of $C_P$

Figure 13: Mean pressure coefficient profiles: baseline LES (black dots) and sensitivity intervals (gray area) compared to the wind tunnel data (red circles).

To identify the main effect associated with each uncertain inflow parameter, Figure 14 shows the profiles of the mean pressure coefficients obtained by averaging across simulations that have a fixed value for one of the uncertain inflow parameters. Figures 14a and 14b compare profiles of $C_P$ averaged across the simulations with the same values of $y_0$. The largest effect of the roughness length occurs inside the separation region, where $C_P$ experiences a maximum variation of $\sim 0.06$ (i.e. $\sim 8\%$), in both rows of taps considered. In general, lower values of $y_0$ are associated with higher negative values of mean $C_p$. The sensitivity of the mean $C_p$ on the turbulence kinetic energy and integral time-scale appears negligible.

#### *4.3.2. Rms pressure coefficient*

Figure 15 plots the distribution of the rms pressure coefficient. Both the experiment and the baseline LES manifest an increase in $C_p'$ where reattachment occurs in the mid portion of the model (Figures 15a and 15b). The highest value of $C_p'$ occurs near the upper edge of the model, where a maximum value of $\sim 0.29$ and $\sim 0.31$ are computed by the experiment and baseline LES, respectively. The maximum discrepancy across the ensemble of 27 LES, shown in Figure 15c, is again largest inside the separation region. The plots indicate that the inflow parameters have stronger influence on $C_p'$, compared to the mean $C_p$: the maximum variation of $\sim 0.16$ across the 27 LES simulations corresponds to $\sim 50\%$ difference.

Figure 16 further quantifies the results, showing rms pressure coefficient profiles along the two rows of taps on tiles A and B. The baseline LES and the sensitivity intervals are compared to the wind tunnel measurements. The $C_p'$ obtained in the PoliMi experiment is fully encompassed by the LES sensitivity intervals in both rows of taps considered. The size of the intervals confirms the high sensitivity of the rms pressure coefficients to the inflow uncertainty. The effect is larger inside the separation and reattachment regions of the flow, compared to the rear portion of the model, where the flow is attached. However, differently from the mean $C_p$, the effect of the inflow uncertainty on the rms $C_p$ appears non-negligible in all locations.

To identify the main effect associated with each uncertain inflow parameter, Figure 17 again shows the profiles obtained by averaging across simulations that

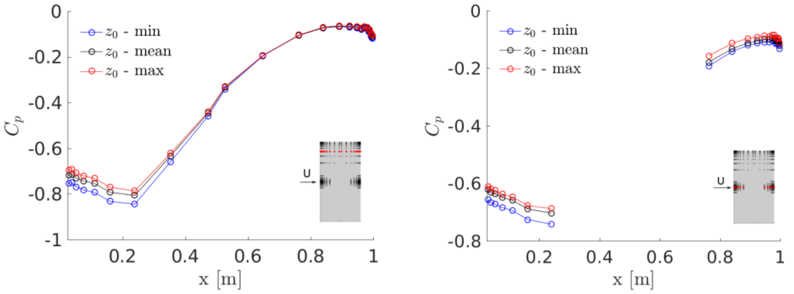

(a) Effect of $y_0$ on tile A (b) Effect of $y_0$ on tile B

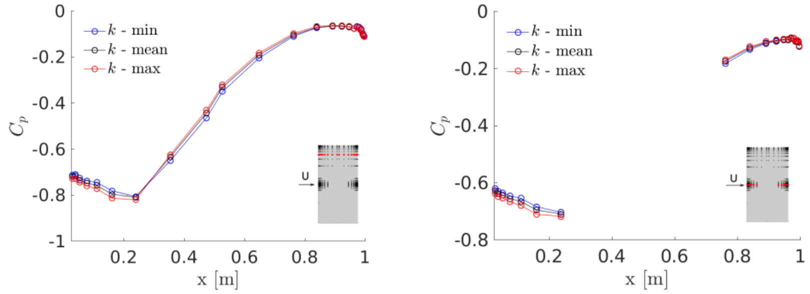

(c) Effect of $k$ on tile A (d) Effect of $k$ on tile B

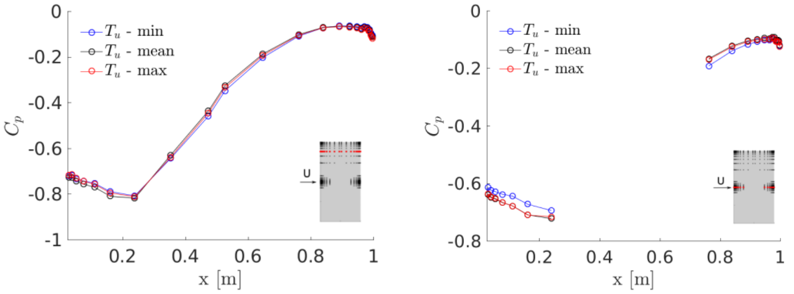

(e) Effect of $T_u$ on tile A (f) Effect of $T_u$ on tile B

Figure 14: Effect of the different uncertain inflow parameters on the mean pressure coefficient profiles. The profiles are obtained by averaging the results of the simulations with a fixed value for one of the parameters, reported in the corresponding label in the legend.

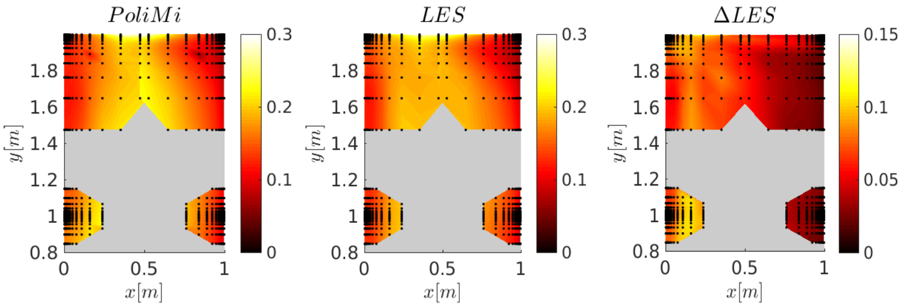

(a) Wind tunnel (b) Baseline LES (c) Maximum discrepancy

Figure 15: Rms pressure coefficient distribution on the building's lateral façade.

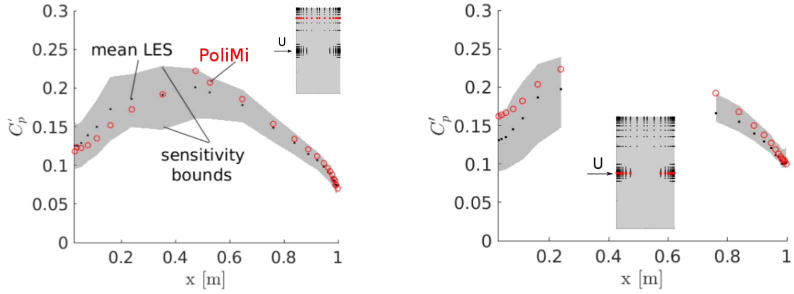

(a) Profiles of $C_p'$ (b) Profiles of $C_p'$

Figure 16: Rms pressure coefficient profiles: baseline LES (black dots) and sensitivity intervals (gray area) compared to the wind tunnel data (red circles).

have a fixed value for one of the uncertain inflow parameters. Figures 17a and 17b compare profiles of $C_p'$ averaged across the simulations with identical values of $y_0$. The profiles on tile A mostly overlap; the maximum variation is $\sim 0.01$ and occurs in the region of flow reattachment. On tile B, the the maximum difference is slightly higher ($\sim$ 0.02), and it arises in the rear portion of the model. Figures 17c and 17d show that the uncertainty in the turbulence kinetic energy primarily influences the $C_p'$ in the front portion of the model, i.e. inside the separation region. Higher values of $C_p'$ are associated with higher values of $k$, and the maximum variation across the profiles is $\sim 0.03$. The effect of $k$ is negligible in the rear portion of the model, where the flow is attached. Lastly, Figures 17e and 17f indicate that the integral time-scale imposed at the inflow causes the largest uncertainty in the $C_p'$, especially inside the separation region. This result has to be interpreted with care: Figures 11h and 11i indicate that the difference in $C_p'$ is a result of the combination of the increased turbulence kinetic energy and the increased integral time scale at the location of the building. This combined effect indicates the importance of accurately quantifying the turbulence statistics at the building location in LES of wind loading.

### *4.3.3. Peak pressure coefficient*

Figure 18 shows the distribution of the peak pressure coefficients relative to a 22% probability of exceedance. Figures 18a and 18b indicate qualitatively good agreement between the experiment and the LES: the largest negative $\check{C}_p$ values are experienced inside the separation region and near the upper edge of the building. Quantitatively, the baseline LES under-predicts the magnitude of the peak pressure coefficients: the minimum $\check{C}_p$ is $-2.5$, compared to $\sim -2.7$ measured in the wind tunnel experiment. However, the minimum values of $\check{C}_p$ across the 27 LES simulations, shown in Figure 18c, reaches values as negative as those found in the experiment, with a minimum $\check{C}_p$ of $\sim -3.1$. Figure 18d plots the local difference between the minimum and maximum values recorded across the 27 LES simulations. The largest uncertainty occurs inside the separation region and next to the upper edge of the building, i.e. in the regions that

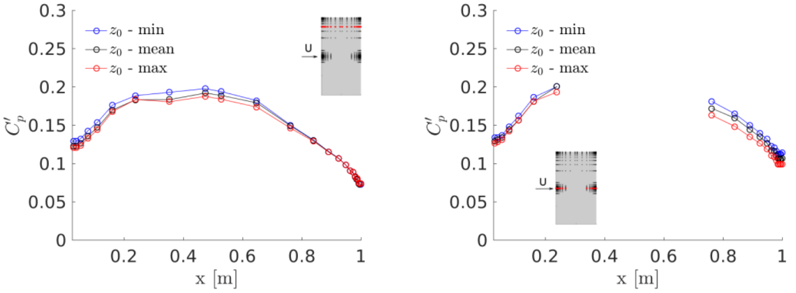

(a) Effect of $y_0$ on tile A (b) Effect of $y_0$ on tile B

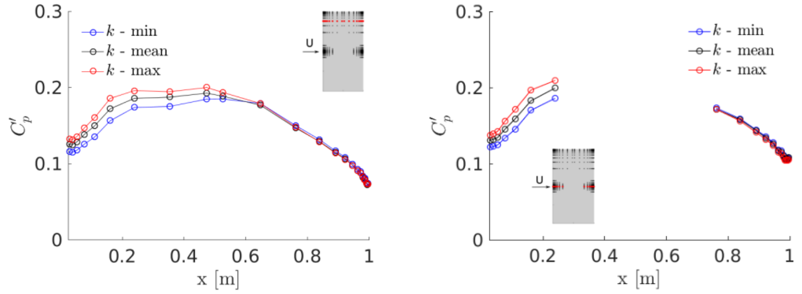

(c) Effect of $k$ on tile A (d) Effect of $k$ on tile B

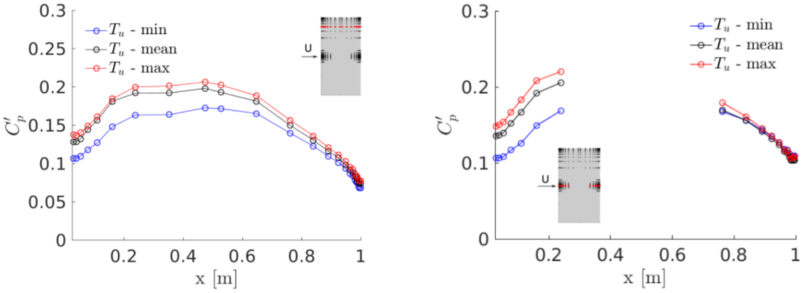

(e) Effect of $T_u$ on tile A (f) Effect of $T_u$ on tile B

Figure 17: Effect of the different inflow parameters on the rms pressure coefficient profiles. The profiles are obtained by averaging the results of the simulations with a fixed value for one of the parameters, reported in the corresponding label in the legend.

experience the highest pressure peaks. Here, the inflow uncertainty can cause variations in $\check{C}_p$ of up to 1.14.

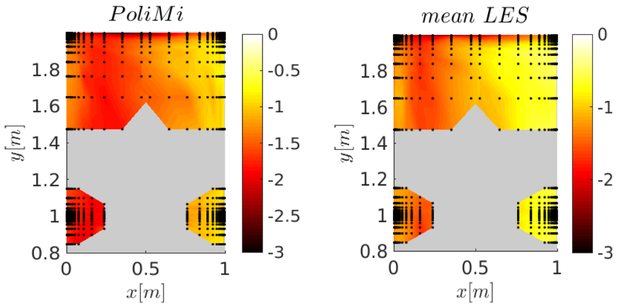

(a) Wind tunnel (b) baseline LES

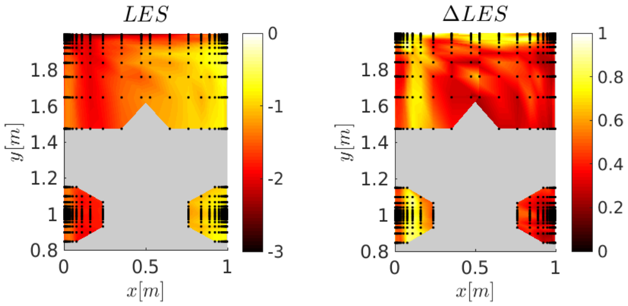

(c) Minimum (d) Maximum discrepancy

Figure 18: Distribution of peak pressure coefficient relative to a 22% probability of exceedance on the building's lateral façade.

Figure 19 further quantifies these results by comparing $\check{C}_p$ profiles along two rows of taps on the building's side wall. The baseline result and the sensitivity intervals are compared to the wind tunnel measurements. The width of the sensitivity intervals indicates that the uncertainty in the inflow conditions significantly affects the $\check{C}_p$ prediction in all locations on the building's lateral façade. Overall, $\sim$ 60% and $\sim$ 5% of the data along the profiles on tiles A and B are encompassed by the sensitivity intervals, respectively. The highest discrepancy between the most negative interval bound and the experimental data is $\sim 0.18$ along the top row and $\sim 0.35$ along the mid row, which correspond to $\sim$ 15% and $\sim$ 20% of $\check{C}_p$, respectively. This under-prediction of the magnitude of local peak values should be expected, since the combination of the filtering operation and numerical dissipation will decrease the peak values calculated from the resolved turbulent pressure signal. This could potentially be addressed by including the contribution of subgrid fluctuations.

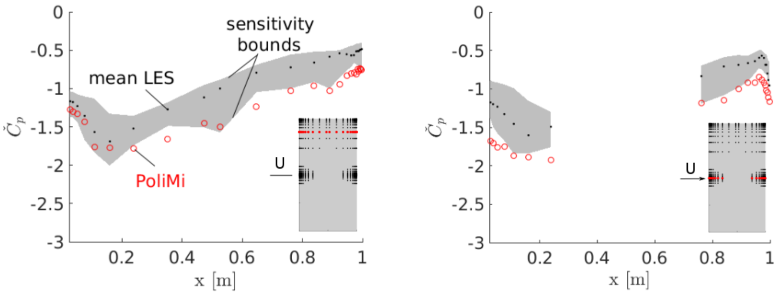

(a) Profiles of $\check{C}_p$ (b) Profiles of $\check{C}_p$

Figure 19: Profiles of peak pressure coefficient relative to a 22% probability of exceedance: baseline LES (black dots) and sensitivity intervals (gray area) compared to the wind tunnel data (red circles).

To identify the main effect associated with each uncertain inflow parameter, Figure 20 compares profiles of $\check{C}_p$ averaged across simulations that have a fixed value for one of the uncertain inflow parameters. The effect of the roughness length, shown in Figures 20a and 20b, is analogous to its effect on the mean pressure coefficient. Variations in $y_0$ can cause up to $\sim 0.14$ (i.e. $\sim 10\%$) variations in the $\check{C}_p$, inside the separation region of the flow. In general, lower $y_0$ values are associated with more negative values of $\check{C}_p$. Figures 20c, 20d, 20e and 20f indicate that the turbulence kinetic energy $k$ and integral time-scale $T_u$ cause a maximum variation of $\sim 0.18$ and $\sim 0.26$, respectively. As for the rms $C_p$, higher values of $k$ or $T_u$ are associated with higher absolute values of peak pressure coefficient. Again, the effect of $T_u$ has to interpreted with care: Figures 11h and 11i indicate that the difference in $\check{C}_p$ is a result of the combination of the increased turbulence kinetic energy and the increased integral time scale at the location of the building.

### *4.3.4. Design pressure coefficient*

The point-wise values for $\check{C}_p$ are not the main quantity of interest for cladding design; instead, the main quantity interest is the design pressure coefficient $\check{C}_{p,d}$ of the panels. $\check{C}_{p,d}$ can be calculated by applying the Cook and Mayne method

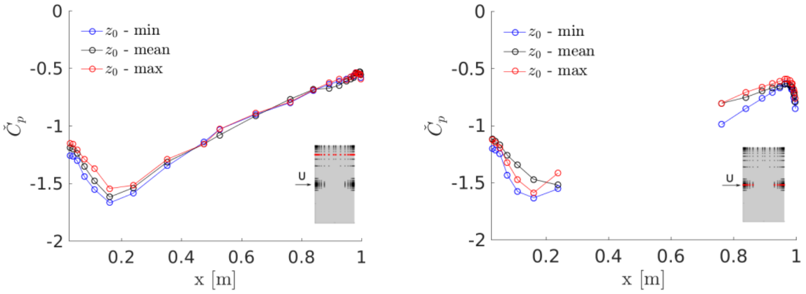

(a) Effect of $y_0$ on tile A (b) Effect of $y_0$ on tile B

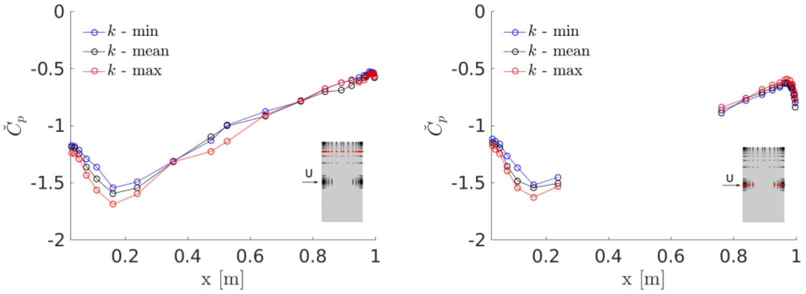

(c) Effect of $k$ on tile A (d) Effect of $k$ on tile B

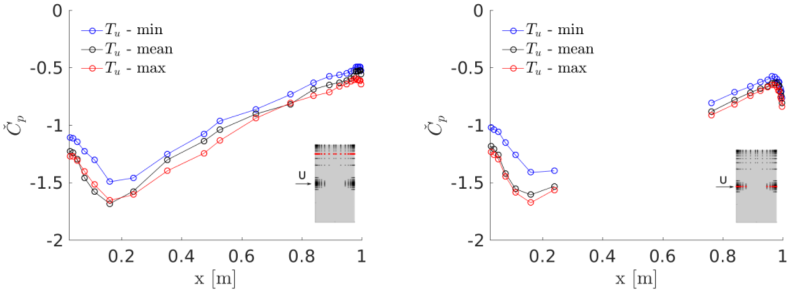

(e) Effect of $T_u$ on tile A (f) Effect of $T_u$ on tile B

Figure 20: Effect of the different inflow parameters on the peak pressure coefficient profiles. The profiles are obtained by averaging the results of the simulations with a fixed value for one of the parameters, reported in the corresponding label in the legend.

[16] to the pressure coefficient averaged over the panel area. Figure 21 plots the resulting extreme value distributions of $C_p$ averaged over a typical $2 \times 3\text{m}^2$ panel, at the top-windward corner of the model, i.e. the most critical region for the considered wind direction. The spread of the cumulative density functions (CDFs) of Figure 21 highlights the importance of the uncertainty in the inflow conditions. The resulting horsetail plot, formed by the ensemble of LES distributions, fully encompasses the experimental distribution. This means that the ensemble of LES can provide an upper and lower bound on the measurement result for any desired probability of exceedance.

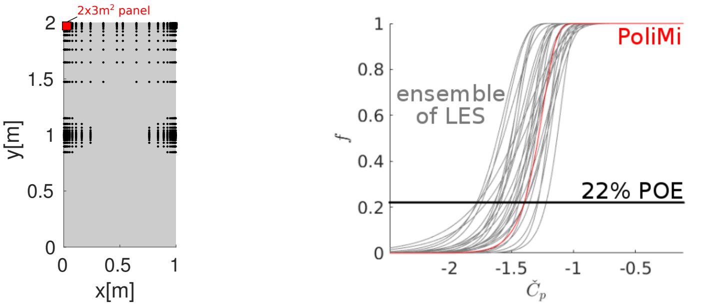

(a) $2 \times 3\text{m}^2$ panel on top corner

(b) Extreme value distributions of $C_{p,AA}$

Figure 21: Cumulative density functions of the extreme values of the pressure coefficient averaged over a $2 \times 3\text{m}^2$ panel.

Lastly, Figure 22b shows the design pressure coefficient relative to a 22% probability of exceedance for panels of increasing dimension, located at the top-windward corner of the building (Figure 22a). For all panel sizes considered, the design pressure coefficient is within the sensitivity intervals predicted by the LES. The magnitude of $\check{C}_{p,d}$ decreases with increasing panel area, meaning that the area-averaging procedure is increasingly filtering out more localized strong negative pressure peaks. These results for $\check{C}_{p,d}$ demonstrate that the effects of the filtering operation and any numerical dissipation in the LES do not deteriorate the prediction of the main quantity of interest for cladding design.

To identify the main effect of each individual uncertain inflow parameter, Figure 23 compares the values for $\check{C}_{p,d}$ as a function of panel size, computed by averaging the results across the simulations that have a fixed value for on of

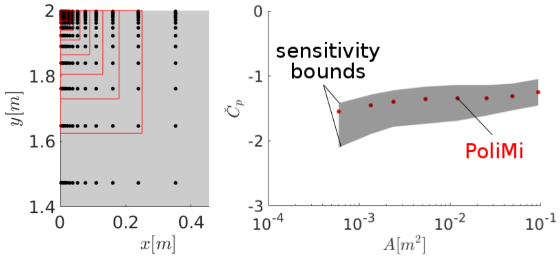

(a) Panels on tile A (b) Profiles of design $C_p$

Figure 22: Design pressure coefficients as a function of panel size.

the inflow parameters. The uncertainty in the roughness length $y_0$ can cause up to $\sim 0.27$ variation in $\check{C}_{p,d}$. The trend is similar to that observed for the peak pressure coefficient: lower terrain roughness is associated with higher absolute values of $\check{C}_{p,d}$. Variations in turbulence kinetic energy produce a maximum variation of $\sim 0.16$ for the selected panel sizes, while the effect of changing the turbulence integral time-scale at the inflow causes a maximum variation of $\sim 0.22$. As before, higher values of the turbulence kinetic energy and integral time-scale at the inflow result in higher absolute values of $\check{C}_{p,d}$; once again, the difference in $\check{C}_{p,d}$ due to a change in the inflow value of $T_u$ is the result of a combination of the increased turbulence kinetic energy and the increased integral time scale at the location of the building.

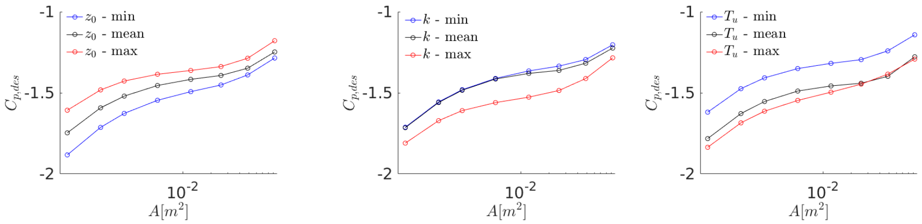

(a) Effect of $y_0$ (b) Effect of $k$ (c) Effect of $T_u$

Figure 23: Effect of the different inflow parameters on the design pressure coefficient profiles. The profiles are obtained by averaging the results of the simulations with a fixed value for one of the parameters, reported in the corresponding label in the legend.

## 5. Conclusions and future work

We have performed 27 LES simulations of a wind tunnel experiment of a high-rise building to analyze sensitivity of the results to uncertainty in the inflow conditions. We identified three uncertain parameters in the inflow conditions, i.e. the roughness length of the terrain, the turbulence kinetic energy and the streamwise integral time-scale. By analyzing measurements performed at different spanwise locations on the wind tunnel turntable, we defined minimum, mean and maximum values for these three parameters, resulting in 27 different inflow conditions. The analysis of the result focused on determining the effect of the inflow conditions on the mean, rms and peak pressure coefficients distribution on the building, and on the design pressure coefficient for cladding panels of different sizes.

Initial analysis of the baseline LES indicates that the LES does not capture as small scales as the experiment, but it does produce strong negative pressure peaks with a similar magnitude and spatial characteristic as the experiment. Simultaneous visualizations of the instantaneous pressure coefficient distribution and coherent structures in the flow showed a correlation between peak events and the presence of turbulent structures.

Subsequently, we analyzed the effect of the inflow conditions on the turbulence statistics at the building location. It was shown that the 27 simulations are representative of the uncertainty in the wind tunnel measurements. The terrain roughness length primarily affects the mean velocity at the building location, while changes in the turbulence kinetic energy and integral time-scale at the inflow, primarily affect the velocity fluctuations further downstream. Importantly, changes in the integral time-scale at the inflow were shown to affect both the value of the turbulence kinetic energy and the integral time-scale at the building location.

The comparison of the mean and rms pressure coefficients showed good agreement between the experiment and numerical simulations, despite a slight under-estimation of the magnitude of the mean pressure coefficient. To study the main effect of the inflow parameters, we averaged the results across simulations with a fixed value for one of the uncertain parameters. This highlighted that the roughness length primarily affects the mean pressure coefficients, while the turbulence kinetic energy and integral time scale primarily affect the rms pressure coefficients. In particular, lower terrain roughness is associated with more negative mean pressure coefficients, while a larger turbulence kinetic energy or integral time-scale produce higher rms pressure coefficients. In both cases, the effects are strongest in the separation region and near the point of reattachment. It was noted that the effect of the integral time-scale on the rms pressure coefficients is a result of the combination of the increased turbulence kinetic energy and the increased integral time scale at the location of the building. This combined effect indicates the importance of accurately quantifying the turbulence statistics at the building location, rather than at the inflow, in LES of wind loading.

Lastly, we performed extreme value analysis to compute the distribution of the peak pressure coefficient on the building's façade, and the design pressure coefficients for cladding panels of different size. By accounting for the uncertainty in the inflow conditions, the LES can predict values of peak pressure coefficient as negative as the ones found in the experiment, although the magnitude of the local peak pressure coefficients is on average under-predicted by 12%. This under-prediction can be explained by the effect of the filtering operation and numerical dissipation in the LES. When considering design pressure coefficients on cladding panels of different sizes located at the upper-windward corner of the building, these effects become less important: the LES sensitivity analysis provides an interval that encompasses the experimental result. It was shown that all inflow parameters significantly contribute to the uncertainty in the peak and design pressure coefficients. The importance of the roughness length can be explained by its effect on the shear in the mean velocity profile, and consequently on the mean pressure coefficient. The effect of the turbulence kinetic energy and the integral time-scale is analogous to their effect on the rms pressure coefficients.

In summary, we can conclude that uncertainty in the ABL inflow statistics, such as those occurring during well controlled wind tunnel experiments, can cause significant uncertainty in the mean, rms and peak pressure distributions and in the design pressure coefficients on high-rise buildings' façades. By accurately characterizing the LES ABL statistics at the building location, and accounting for inflow uncertainty when performing validation against experiments, the confidence in LES predictions for wind loading could be drastically increased. Future work will focus on the potential benefits of using a more advanced subgrid model, such as the dynamic $k$-equation model, particularly when considering local peak pressure coefficients. Furthermore, we plan to perform additional LES simulations for different wind directions, including those for which the wind tunnel experiment observed the occurrence of very strong, localized pressure peak events.

## 6. Acknowledgements

This material is based upon work supported by the National Science Foundation under Grant Number 1635137, and used the Extreme Science and Engineering Discovery Environment (XSEDE), which is supported by National Science Foundation grant number CI-1548562.

[1] JD Holmes. Non-gaussian characteristics of wind pressure fluctuations. *Journal of Wind Engineering and Industrial Aerodynamics*, 7(1):103–108, 1981.

[2] D Surry and D Djakovich. Fluctuating pressures on models of tall buildings. *Journal of Wind Engineering and Industrial Aerodynamics*, 58(1-2):81–112, 1995.

[3] Dae Kun Kwon and Ahsan Kareem. Peak factors for non-gaussian load effects revisited. *Journal of Structural Engineering*, 137(12):1611–1619, 2011.

[4] Fahim Sadek and Emil Simiu. Peak non-gaussian wind effects for database-assisted low-rise building design. *Journal of Engineering Mechanics*, 128(5):530–539, 2002.

[5] Xinlai Peng, Luping Yang, Eri Gavanski, Kurtis Gurley, and David Prevatt. A comparison of methods to estimate peak wind loads on buildings. *Journal of wind engineering and industrial aerodynamics*, 126:11–23, 2014.

[6] Nicholas J Cook. on the gaussian-exponential mixture model for pressure coefficients. *Journal of Wind Engineering and Industrial Aerodynamics*, 153:71–77, 2016.

[7] D Surry and T Stathopoulos. An experimental approach to the economical measurement of spatially-averaged wind loads. *Journal of Wind Engineering and Industrial Aerodynamics*, 2(4):385–397, 1978.

[8] WH Melbourne. Comparison of measurements on the caarc standard tall building model in simulated model wind flows. *Journal of Wind Engineering and Industrial Aerodynamics*, 6(1-2):73–88, 1980.

[9] JD Holmes. Distribution of peak wind loads on a low-rise building. *Journal of Wind Engineering and Industrial Aerodynamics*, 29(1-3):59–67, 1988.

[10] J E Cermak. Wind-tunnel development and trends in applications to civil engineering. *Journal of wind engineering and industrial aerodynamics*, 91(3):355–370, 2003.

[11] F Cluni, V Gusella, SMJ Spence, and G Bartoli. Wind action on regular and irregular tall buildings: Higher order moment statistical analysis by hffb and smpss measurements. *Journal of Wind Engineering and Industrial Aerodynamics*, 99(6-7):682–690, 2011.

[12] W Kim, Y Tamura, and A Yoshida. Interference effects on local peak pressures between two buildings. *Journal of Wind Engineering and Industrial Aerodynamics*, 99(5):584–600, 2011.

[13] MF Huang, W Lou, C M Chan, N Lin, and X Pan. Peak distributions and peak factors of wind-induced pressure processes on tall buildings. *Journal of Engineering Mechanics*, 139(12):1744–1756, 2013.

[14] JW Zhang and QS Li. Field measurements of wind pressures on a 600 m high skyscraper during a landfall typhoon and comparison with wind tunnel test. *Journal of Wind Engineering and Industrial Aerodynamics*, 175:391–407, 2018.

[15] TV Lawson. The design of cladding. *Building and Environment*, 11(1):37–38, 1976.

[16] NJ Cook and JR Mayne. A refined working approach to the assessment of wind loads for equivalent static design. *Journal of Wind Engineering and Industrial Aerodynamics*, 6(1-2):125–137, 1980.

[17] John Dean Holmes. Equivalent time averaging in wind engineering. *Journal of Wind Engineering and Industrial Aerodynamics*, 72:411–419, 1997.

[18] L. Amerio. *Experimental high resolution analysis of the pressure peaks on a building scale model façades*. PhD thesis, Politecnico di Milano, 2018.

[19] Stephen B Pope. Turbulent flows, 2001.

[20] Luca Bruno, Maria Vittoria Salvetti, and Francesco Ricciardelli. Benchmark on the aerodynamics of a rectangular 5: 1 cylinder: an overview after the first four years of activity. *Journal of Wind Engineering and Industrial Aerodynamics*, 126:87–106, 2014.

[21] Marie Skytte Thordal, Jens Chr Bennetsen, and H Holger H Koss. Review for practical application of cfd for the determination of wind load on high-rise buildings. *Journal of Wind Engineering and Industrial Aerodynamics*, 186:155–168, 2019.

[22] Hee Chang Lim, TG Thomas, and Ian P Castro. Flow around a cube in a turbulent boundary layer: Les and experiment. *Journal of Wind Engineering and Industrial Aerodynamics*, 97(2):96–109, 2009.

[23] Agerneh K Dagnew and Girma T Bitsuamlak. Computational evaluation of wind loads on a standard tall building using les. *Wind and Structures*, 18(5):567–598, 2014.

[24] H. Aboshosha, A. Elshaer, G. T. Bitsuamlak, and A. El Damatty. Consistent inflow turbulence generator for les evaluation of wind-induced responses for tall buildings. *Journal of Wind Engineering and Industrial Aerodynamics*, 142:198–216, 2015.

[25] L Patruno, M Ricci, S De Miranda, and F Ubertini. Numerical simulation of a 5: 1 rectangular cylinder at non-null angles of attack. *Journal of Wind Engineering and Industrial Aerodynamics*, 151:146–157, 2016.

[26] M Ricci, L Patruno, I Kalkman, S de Miranda, and B Blocken. Towards les as a design tool: Wind loads assessment on a high-rise building. *Journal of Wind Engineering and Industrial Aerodynamics*, 180:1–18, 2018.

[27] Shenghong Huang, QS Li, and Shengli Xu. Numerical evaluation of wind effects on a tall steel building by cfd. *Journal of Constructional Steel Research*, 63(5):612–627, 2007.

[28] Steven J Daniels, Ian P Castro, and Zheng-Tong Xie. Peak loading and surface pressure fluctuations of a tall model building. *Journal of Wind Engineering and Industrial Aerodynamics*, 120:19–28, 2013.

[29] A. Keating, U. Piomelli, E. Balaras, and H.J. Kaltenbach. A priori and a posteriori tests of inflow conditions for large-eddy simulation. *Physics of Fluids*, 16(12):4696–4712, 2004.

[30] N Jarrin, R Prosser, J-C Uribe, S Benhamadouche, and D Laurence. Reconstruction of turbulent fluctuations for hybrid rans/les simulations using a synthetic-eddy method. *International Journal of Heat and Fluid Flow*, 30(3):435–442, 2009.

[31] G. Lamberti, C. García-Sánchez, J. Sousa, and C. Gorlé. Optimizing turbulent inflow conditions for large-eddy simulations of the atmospheric boundary layer. *Journal of Wind Engineering and Industrial Aerodynamics*, 177:32–44, 2018.

[32] Y. Kim, I. P. Castro, and Z. T. Xie. Divergence-free turbulence inflow conditions for large-eddy simulations with incompressible flow solvers. *Computers & Fluids*, 84:56–68, 2013.

[33] G. Lamberti, L. Amerio, G. Pomaranzi, A. Zasso, and C. Gorlé. Comparison of high resolution pressure measurements on a high-rise building in a closed and open-section wind tunnel. *Journal of wind engineering and industrial aerodynamics*, (under review).

[34] J Smagorinsky. General circulation experiments with the primitive equations: I. the basic experiment. *Monthly weather review*, 91(3):99–164, 1963.

[35] Jörg Franke. *Best practice guideline for the CFD simulation of flows in the urban environment.* Meteorological Inst., 2007.

[36] W Cabot and P Moin. Approximate wall boundary conditions in the large-eddy simulation of high reynolds number flow. *Flow, Turbulence and Combustion*, 63:269–291, 1999.

[37] Z. T. Xie and I. P. Castro. Efficient generation of inflow conditions for large eddy simulation of street-scale flows. *Flow, turbulence and combustion*, 81(3):449–470, 2008.

[38] PJ Richards and BS Wanigaratne. A comparison of computer and wind-tunnel models of turbulence around the silsoe structures building. *Journal of Wind Engineering and Industrial Aerodynamics*, 46:439–447, 1993.

[39] A. Parente, C. Gorle, J. van Beeck, and C. Benocci. Improved kappa-epsilon model and wall function formulation for the RANS simulation of ABL flows. *Journal of Wind Engineering and Industrial Aerodynamics*, 99:267–278, 2011.

[40] G. I. Taylor. The spectrum of turbulence. In *Proceedings of the Royal Society of London A: Mathematical, Physical and Engineering Sciences*, volume 164, pages 476–490. The Royal Society, 1938.

[41] Peter Welch. The use of fast fourier transform for the estimation of power spectra: a method based on time averaging over short, modified periodograms. *IEEE Transactions on audio and electroacoustics*, 15(2):70–73, 1967.

[42] V. Holmén. Methods for vortex identification. *Master's Theses in Mathematical Sciences*, 2012.

[43] PJ Saathoff and WH Melbourne. The generation of peak pressures in separated/reattaching flows. *Journal of Wind Engineering and Industrial Aerodynamics*, 32(1-2):121–134, 1989.